Chapter 3

Simplified Analytical Analysis of Axial Flux Permanent Magnet Machine with Saturated Teeth

3.1 Introduction

The inherent pancake shape of the Axial Flux Permanent Magnet (AFPM) machine ensures compact construction and improves its power density. The aided advantage of high power density and compact shape promotes the AFPM machine for various applications such as pumps, fans, electric vehicle motor and wind power generators. All possible variants of AFPM viz., single sided, double sided and multi stacked intact its compactness and robustness. Moreover, AFPM topologies offer the feasibility to design a high pole machine, which is an additional advantage to low speed direct drive applications such as electric vehicle and direct drive wind power generator. Because of all aforementioned features, AFPM machine is considered as an alternative to the cylindrical radial flux PM machine for applications including electric vehicle, wind power generator, machining spindles, dental drills, fans, compressors, ship propeller etc. Besides this, the specific applications such as flywheel motor/generator set, which need high rotor inertia to store kinetic energy prefers AFPM machine. It is because the inertia of an axial-flux machine is easier to adjust than its radial-flux counterpart and the thickness of the rotor can be adjusted in axial length without affecting the electromagnetic performance of the machine.

At early stage of design, it is essential to have prior knowledge of machine's parameters such as cogging torque, Back EMF, winding inductances and average torque. These information can be evaluated using solution of Maxwell equations. The AFPM analysis is inherently a 3D electromagnetic field problem. The accurate results can be obtained with 3-D finite-element method (FEM). Significant amount of work has been done so far for the estimation of AFPM machine's performance. The researchers [151] and [152] have exploited integral transform method and the free-space Greens function method, respectively as three dimensional analysis of the slotless AFPM machine. Recently, in papers [153] and [154], the authors developed analytical model for analysis of AFPM and radial flux machine using Fourier transform. These techniques helped to achieve significantly high accuracy with increased complexity to accuracy ratio. Further attempts are made to find exact solution of AFPM machine using Fourier series [155]- [159], but these are limited to slotless machine. Moreover, the authors in [158] and [159] considered periodicity in peripheral and axial direction. The solution ended up with modified Bessel function in radial direction. Hence, these solutions resulted into double Fourier series. On the other hand, to keep intact the advantages of the analytical model, several works have been carried out to simplify the modeling. In order to reduce the computational complexity, actual 3D geometry of machine given in the Figure-3.1 is cut axially and unrolled to make its linear counter part [160]- [162]. The linear equivalent of AFPM machine is shown in the Figure-3.2. This simplification converts 3D complex problem in 2D in $z\theta$- plan,

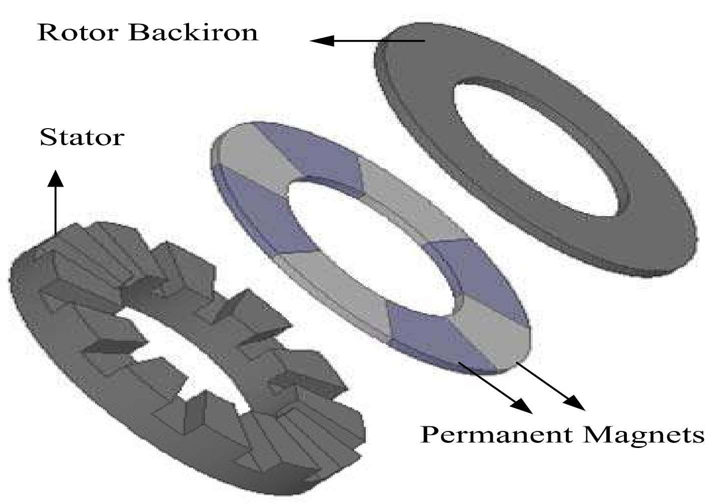

Figure 3.1: Axial Flux Permanent Magnet Machine

however, the flux density of AFPM machine is radius dependent and in 2D approximation this dependency is lost. Due to this, the analytical results agree with FEM at the mean

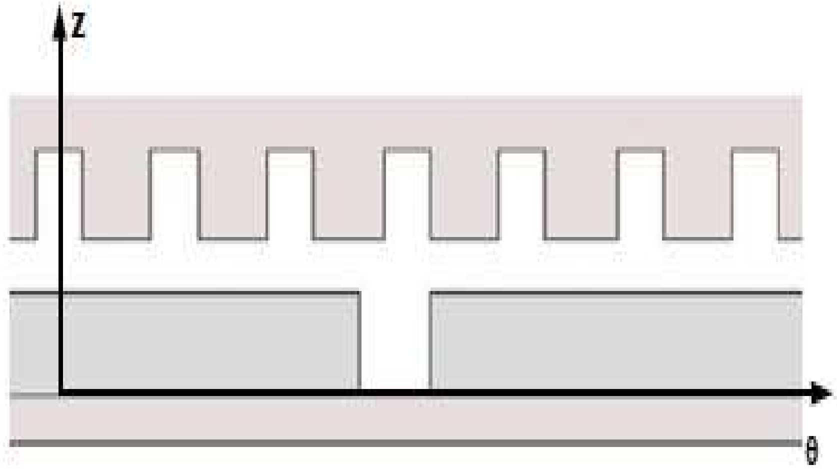

Figure 3.2: Linear Equivalent of Axial Flux Permanent Magnet Machine

radius of the machine, whereas the accuracy degrades with radial position. This happens due to flux fringing at inner and outer radii of the machine. Hence, this approximation reduces the accuracy of the analysis and high discrepancy can be observed with large machine. However, improved analytical models have been proposed to take account of the radial dependency of the analysis [163]. This method extended the two-dimensional (2-D) solution of Maxwell equations to a 3-D case by multiplying a radial dependent function obtained from a FEM study. Subsequently, the authors [164] comprehensively described the method for determining the radial dependent function. Further improvement in the analysis is reported using method of multi-slice [165]. In this method, the machine was considered as a combination of several linear machines (several slices), and solution of each slice is evaluated using a 2-D linear modeling.

All the reported analysis consider the tooth of the stator core to be infinitely permeable, however, the combined effects of armature current, and permanent magnet saturates the stator core. This significantly influences the machine behaviour. Moreover, the obtained no-load machine parameters such as cogging torque, back EMF and winding inductance, and their influence in the machine behaviour under loaded conditions are significantly different. To account the magnetic saturation, reported articles [141], [143]-[144] used the Frozen Permeable technique, which has been discussed in the Chapter 2. However, this method is highly accurate, but is highly time consuming and needs huge computational memory to store magnetic properties of every elements at each step time of the simulated model. In order to restore the benefits of the analytical modeling, an analytical model is proposed in this chapter to take account of finite permeability of teeth in magnetically saturated AFPM machine. The proposed analytical model is verified with the FEM results obtained from Ansys Maxwell Software.

3.2 Analytical Model for Axial Flux Open Slot Permanent Magnet Machine

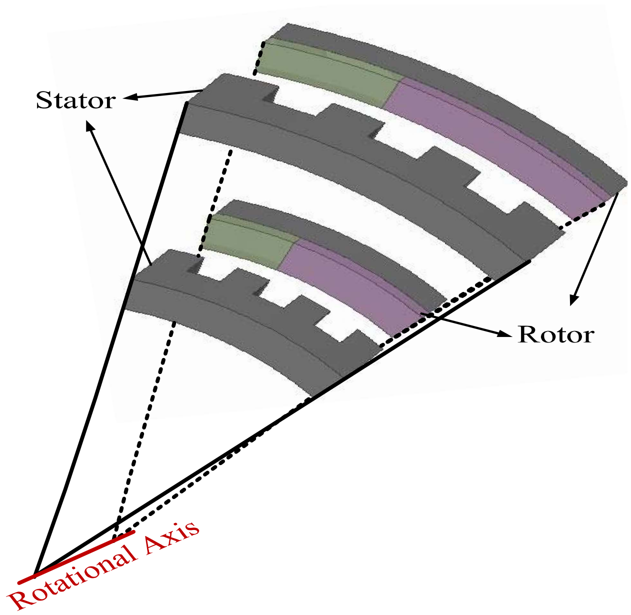

Figure 3.3: Demonstration of Multislice Slice Approach for AFPM Machine

In order to develop analytical solution, the multislice method is used to reduce the 3D problem into 2D. According to multislice method, the AFPM machine can be divided into several slices as shown in the Figure-3.3, and linear model analysis of these slices can be used for the performance evaluation. Due to symmetry, end effects are ignored. In the present analysis, arbitrary k^{th} slice is considered and a linear model for this slice is developed. The overall performance of the machine is determined using superposition of the performances of every slices. The linear model of the k^{th} slice with finite teeth permeability is shown in the Figure-3.4.

3.2.1 No load Vector Potential Calculation

For foregoing analysis, following assumptions are made :

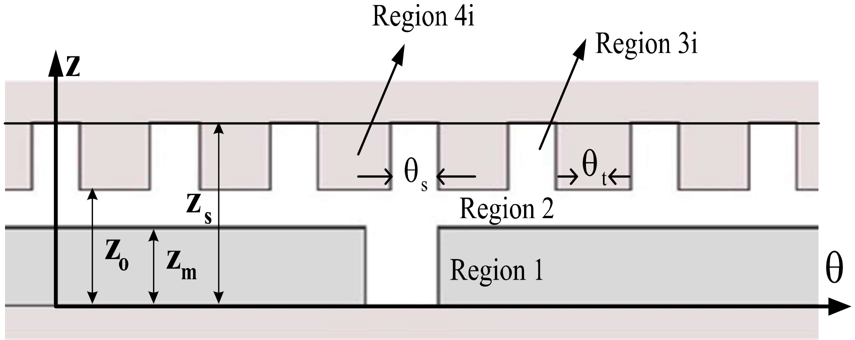

Figure 3.4: Linear Model for k^{th} Slice for AFPM Machine with Finite Permeable Teeth

1. Teeth is considered to be of finite permeability , whose relative permeability is μ_i.

2. PMs is considered to have linear demagnetization curve.

3. Stator yoke, and the rotor core are considered to be unsaturated.

For the investigation of the model shown in the Figure-3.4, whole machine is divided into $(2 + 2Q)$ subregions viz., 1) region 1: permanent magnets region, 2) region 2 : airgap region, 3) region 3i: slot region, and 4) region 4i: tooth region, where $i \in \{1, Q\}$. The coordinate frame is attached to the middle of reference slot as shown in the Figure-3.4, the initial position of i^{th} slot and i^{th} teeth is given as

$$\begin{aligned} \theta_i &= \frac{-\theta_s}{2} + \frac{2i\pi}{Q} \\ \beta_i &= \frac{\theta_s}{2} + \frac{2i\pi}{Q} \end{aligned} \tag{3.1}$$

where, θ_s is slot angle, teeth angle θ_t is defined as $\theta_t = \frac{2\pi}{Q} - \theta_s$, whereas θ_i and β_i are initial position of slot and teeth, and i represents the slot/teeth number. The magnetization pattern in the selected coordinate frame is shown in the Figure-3.5. Though the magnetization distribution is periodic function of period π/p, the slot in the stator generates other harmonics. In order to take account of the all space harmonics, the magnetization distribution patterns is expanded as Fourier series with periodicity of 2π, which is mathematically represented as

$$\mathbf{M_z} = \sum_{n=1,2,3..}^{\infty} M_n \mathrm{cos}n\left(\theta + \theta_o\right) \tag{3.2}$$

where,

$$M_n = \begin{cases} \frac{4P\mathbf{B_r}}{\mu_o n\pi} \sin\left(\frac{n\pi\alpha_p}{p}\right) & \text{if } \ \mathrm{n = jp}, \ \ \mathrm{j} = 1, 3, 5.... \\ 0 & \text{otherwise} \end{cases} \tag{3.3}$$

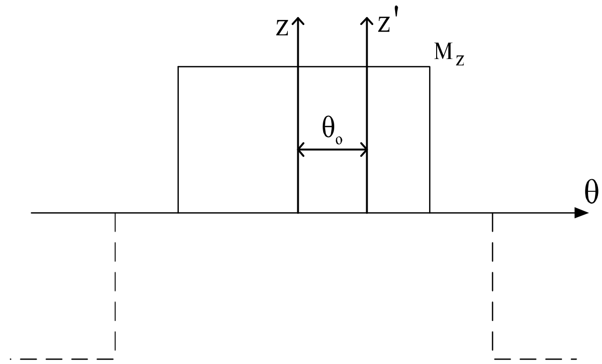

Figure 3.5: Magnetization Distribution

where, B_r is remanence flux density of the magnet and α is the magnet pitch to pole pitch ratio. The governing equations in all multi-regions are established using magnetic vector potential $\mathbf{A}$. The vector potential $\mathbf{A}$ is defined as $\mathbf{B} = \nabla \times \mathbf{A}$, and hence the axial and tangential components of flux density are expressed in terms of vector potential as

$$\mathbf{B_z} = -\frac{1}{r}\frac{\partial \mathbf{A}}{\partial \theta} \tag{3.4}$$

and,

$$\mathbf{B}_\theta = \frac{\partial \mathbf{A}}{\partial z} \tag{3.5}$$

The governing equation in region 1, which lies between $z \in [0, z_m]$, and $\theta \in [0, 2\pi]$ is given as

$$\nabla^2 \mathbf{A_{1n}} = -\mu_o \nabla \times \mathbf{M} \tag{3.6}$$

The region 2 is bounded by $z \in [z_m, z_o]$, and $\theta \in [0, 2\pi]$, and the governing field equation is given by

$$\nabla^2 \mathbf{A_{2n}} = 0 \tag{3.7}$$

The slot region 3i is given by $z \in [z_o, z_s]$, and $\theta \in [\theta_i, \theta_i + \theta_s]$, while the teeth region 4i is bounded by $z \in [z_o, z_s]$, and $\theta \in [\theta_i + \theta_s, \theta_i + \theta_s + \theta_t]$ and their governing field equations are given by

$$\begin{aligned} \nabla^2 \mathbf{A_{3i}} &= 0 \\ \nabla^2 \mathbf{A_{4i}} &= 0 \end{aligned} \tag{3.8}$$

The magnetization distribution expressed in the equation (3.2) is used to simply the poissonian equation (3.6), and variable separable method is used to solve the equations (3.6)-(3.8).

Effectively, for two dimensional analysis of the axial flux machine, the above governing field equations are expanded as follow,

$$\frac{1}{R^2}\frac{\partial^2 \mathbf{A_{1n}}}{\partial \theta^2} + \frac{\partial^2 \mathbf{A_{1n}}}{\partial z^2} = \frac{\mu_o n \mathbf{M_n}}{R} \sin n\left(\theta + \theta_0\right) \tag{3.9}$$

$$\frac{1}{R^2}\frac{\partial^2 \mathbf{A_{2n}}}{\partial \theta^2} + \frac{\partial^2 \mathbf{A_{2n}}}{\partial z^2} = 0 \tag{3.10}$$

$$\frac{1}{R^2}\frac{\partial^2 \mathbf{A_{3i}}}{\partial \theta^2} + \frac{\partial^2 \mathbf{A_{3i}}}{\partial z^2} = 0 \tag{3.11}$$

and,

$$\frac{1}{R^2}\frac{\partial^2 \mathbf{A_{4i}}}{\partial \theta^2} + \frac{\partial^2 \mathbf{A_{4i}}}{\partial z^2} = 0 \tag{3.12}$$

To evaluate the complete solution of the governing field equations (3.9)-(3.12), it is essential to consider the boundary conditions at the interface of media. The boundary condition at the interface of rotor inner surface enforces zero magnetic field intensity as rotor core is assumed to be infinitely permeable. This is mathematically expressed as

$$\left.\frac{\partial \mathbf{A_{1n}}}{\partial z}\right|_{z=0} = 0 \tag{3.13}$$

The general solution of the partial differential equation (3.9) subjected to above boundary condition is given by

$$\mathbf{A_{1n}} = \sum_{n=1,2,3..}^{\infty} \frac{R}{n}\left(a_{1n}\cosh\frac{nz}{R} + G_n\right)\cos n\theta + \sum_{n=1,2,3..}^{\infty} \frac{R}{n}\left(c_{1n}\cosh\frac{nz}{R} + H_n\right)\sin n\theta \tag{3.14}$$

where, $G_n = \mu_o \mathbf{M_n} \sin n\theta_o$, and $H_n = \mu_o \mathbf{M_n} \cos n\theta_o$. Considering the stator yoke to be infinitely permeable, and the flux falls normally at lateral edge of the slot, the following boundary conditions emerged in terms of vector potential,

$$\begin{aligned} \left.\frac{\partial \mathbf{A_{3i}}}{\partial z}\right|_{z=z_s} &= 0 \\ \left.\frac{\partial \mathbf{A_{3i}}}{\partial \theta}\right|_{\theta=\theta_i} &= 0 \\ \left.\frac{\partial \mathbf{A_{3i}}}{\partial \theta}\right|_{\theta=\theta_i+\theta_s} &= 0 \end{aligned} \tag{3.15}$$

and, subsequently, the general solution of the equation (3.11) under above boundary condition is given as

$$\mathbf{A_{3i}} = a_{3o}^i + \sum_{m=1}^{\infty} a_{3m}^i \frac{R\theta_s}{m\pi} \frac{\cosh\left(\frac{m\pi}{R\theta_s}\left(z - z_s\right)\right)}{\cosh\left(\frac{m\pi}{R\theta_s}\left(z_o - z_s\right)\right)} \cos\left(\frac{m\pi}{\theta_s}\left(\theta - \theta_i\right)\right) \tag{3.16}$$

similarly, boundary conditions imposed on the stator teeth are given as

$$\begin{aligned}\left.\frac{\partial \mathbf{A_{4i}}}{\partial z}\right|_{z=z_s} &= 0\\ \left.\frac{\partial \mathbf{A_{4i}}}{\partial \theta}\right|_{\theta=\theta_i+\theta_s} &= 0\\ \left.\frac{\partial \mathbf{A_{4i}}}{\partial \theta}\right|_{\theta=\theta_i+\theta_s+\theta_t} &= 0\end{aligned} \tag{3.17}$$

and, the general solution of the equation (3.12) under above boundary condition is given as

$$\mathbf{A_{4i}} = a^i_{4o} + \sum_{k=1}^{\infty} a^i_{4k} \frac{R\theta_t}{k\pi} \frac{\cosh\left(\frac{k\pi}{R\theta_t}(z-z_s)\right)}{\cosh\left(\frac{k\pi}{R\theta_t}(z_o-z_s)\right)} \cos\left(\frac{k\pi}{\theta_t}(\theta-\theta_i-\theta_s)\right) \tag{3.18}$$

and, the continuity of normal flux density and tangential flux intensity at interface of magnets and airgap is given as

$$\begin{aligned}\mathbf{A_{1n}} &= \left.\mathbf{A_{2n}}\right|_{z=z_m}\\ \frac{\partial \mathbf{A_{1n}}}{\partial z} &= \left.\frac{\partial \mathbf{A_{2n}}}{\partial z}\right|_{z=z_m}\end{aligned} \tag{3.19}$$

finally, the general solution of the equation (3.10) is given as

$$\mathbf{A_{2n}} = \sum_{n=1,2,3..}^{\infty} \frac{R}{n}\left(a_{2n}\cosh\frac{nz}{R} + b_{2n}sinh\frac{nz}{R}\right)\cos n\theta + \sum_{n=1,2,3..}^{\infty} \frac{R}{n}\left(c_{2n}\cosh\frac{nz}{R} + d_{2n}sinh\frac{nz}{R}\right)\sin n\theta \tag{3.20}$$

In the absence of current source at $z = z_o$, the tangential component of magnetic field intensity is continuous, which is expressed as

$$\left.\frac{\partial \mathbf{A_{2n}}}{\partial z}\right|_{z=z_0} = \begin{cases} \frac{\partial \mathbf{A_{3i}}}{\partial z} & \forall\ \theta\ \in\ [\theta_i, \theta_i+\theta_s] \\ \frac{1}{\mu_i}\frac{\partial \mathbf{A_{4i}}}{\partial z} & \forall\ \theta\ \in\ [\theta_i+\theta_s, \theta_i+\theta_s+\theta_t] \end{cases} \tag{3.21}$$

The continuity of the normal flux density at the interface of region 2 and region 3i, and region 2 and region 4i are mathematically expressed as given below

$$\begin{aligned}\mathbf{A_{3i}} &= \left.\mathbf{A_{2n}}\right|_{z=z_0}\\ \mathbf{A_{4i}} &= \left.\mathbf{A_{2n}}\right|_{z=z_0}\end{aligned} \tag{3.22}$$

The coefficients involved in the equations (3.14), (3.16), (3.18) and (3.18) can be evaluated using boundary conditions given by equations (3.19), (3.21), and (3.22) as described in appendix C.

3.2.2 No Load Magnetic Field Calculation

After evaluation of magnetic vector potential in all subdomains, the axial and tangential component of magnetic field density are obtained using formula given in equation (3.4). The axial flux density, and tangential flux density expressions in all sub domains are given as follow:

Region 1

$$\mathbf{B_{1z}} = \sum_{n=1,2,3..}^{\infty} \left(a_{1n}\cosh\frac{nz}{R} + G_n\right)\sin n\theta - \sum_{n=1,2,3..}^{\infty} \left(c_{1n}\cosh\frac{nz}{R} + H_n\right)\cos n\theta \tag{3.23}$$

$$\mathbf{B_{1\theta}} = \sum_{n=1,2,3..}^{\infty} \left(a_{1n}\sinh\frac{nz}{R} + G_n\right)\cos n\theta + \sum_{n=1,2,3..}^{\infty} \left(c_{1n}\sinh\frac{nz}{R} + H_n\right)\sin n\theta \tag{3.24}$$

Region 2

$$\begin{aligned}
\mathbf{B_{2z}} &= \sum_{n=1,2,3..}^{\infty} \left(a_{2n}\cosh\tfrac{nz}{R} + b_{2n}\sinh\tfrac{nz}{R}\right)\sin n\theta \\
&- \sum_{n=1,2,3..}^{\infty} \left(c_{2n}\cosh\tfrac{nz}{R} + d_{2n} sinh \tfrac{nz}{R}\right)\cos n\theta \\
\mathbf{B_{2\theta}} &= \sum_{n=1,2,3..}^{\infty} \left(a_{2n}\sinh\tfrac{nz}{R} + b_{2n}\cosh\tfrac{nz}{R}\right)\cos n\theta \\
&+ \sum_{n=1,2,3..}^{\infty} \left(c_{2n}\sinh\tfrac{nz}{R} + d_{2n}\cosh\tfrac{nz}{R}\right)\sin n\theta
\end{aligned} \tag{3.25}$$

Region 3

$$\begin{aligned}
\mathbf{B_{3iz}} &= -\sum_{m=1}^{\infty} a_{3m}^{i} \frac{\cosh\left(\frac{m\pi}{R\theta_s}(z-z_s)\right)}{\cosh\left(\frac{m\pi}{R\theta_s}(z_o-z_s)\right)} \sin\left(\tfrac{m\pi}{\theta_s}(\theta-\theta_i)\right) \\
\mathbf{B_{3i\theta}} &= \sum_{m=1}^{\infty} a_{3m}^{i} \frac{\sinh\left(\frac{m\pi}{R\theta_s}(z-z_s)\right)}{\cosh\left(\frac{m\pi}{R\theta_s}(z_o-z_s)\right)} \cos\left(\tfrac{m\pi}{\theta_s}(\theta-\theta_i)\right)
\end{aligned} \tag{3.26}$$

and, **Region 4**

$$\begin{aligned}
\mathbf{B_{4iz}} &= -\sum_{k=1}^{\infty} a_{4k}^{i} \frac{\cosh\left(\frac{k\pi}{R\theta_t}(z-z_s)\right)}{\cosh\left(\frac{k\pi}{R\theta_t}(z_o-z_s)\right)} \sin\left(\tfrac{k\pi}{\theta_t}(\theta-\theta_i-\theta_s)\right) \\
\mathbf{B_{4i\theta}} &= \sum_{k=1}^{\infty} a_{4k}^{i} \frac{\sinh\left(\frac{k\pi}{R\theta_t}(z-z_s)\right)}{\cosh\left(\frac{k\pi}{R\theta_t}(z_o-z_s)\right)} \cos\left(\tfrac{k\pi}{\theta_t}(\theta-\theta_i-\theta_s)\right)
\end{aligned} \tag{3.27}$$

3.2.3 Cogging Torque Calculation

The interaction of permanent magnets and teeth of the machine results in the cogging torque. This torque varies with the angular position of the rotor and present even in

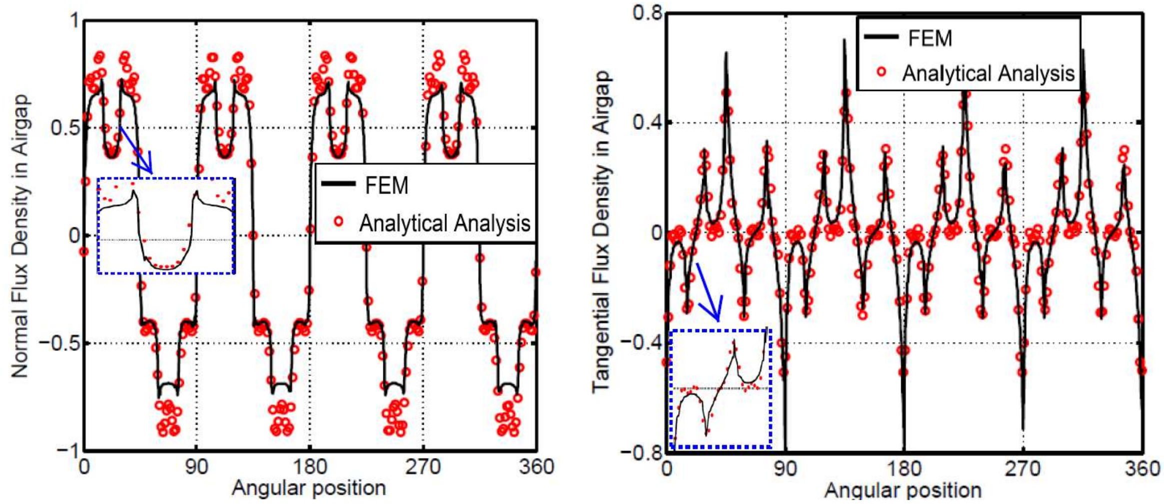

(a) Axial Component (b) Tangential Component

Figure 3.6: Airgap Flux Density Corresponding to $\mu_j = 10$

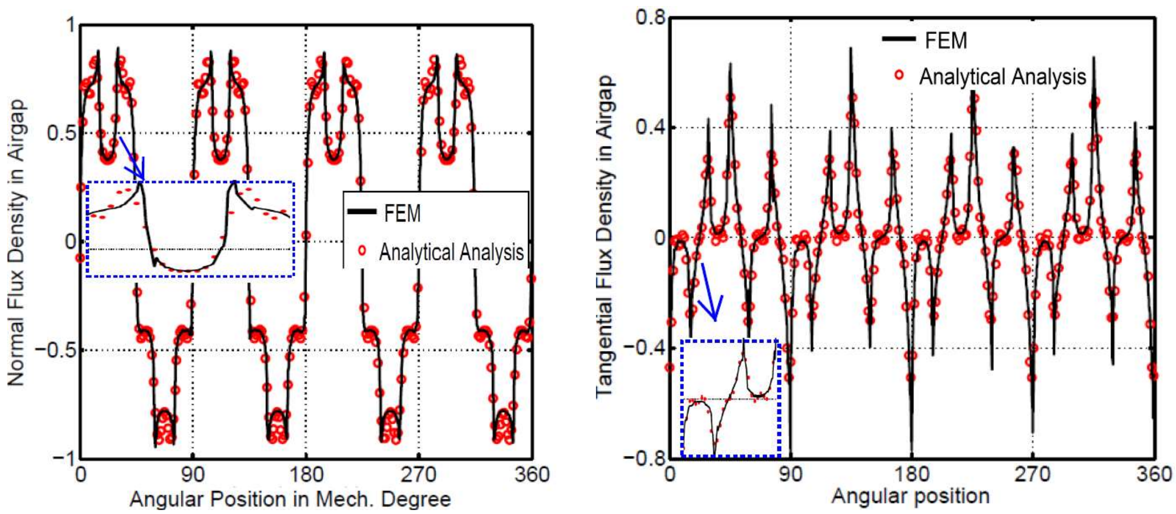

(a) Axial Component (b) Tangential Component

Figure 3.7: Airgap Flux Density Corresponding to $\mu_j = 50$

absence of armature excitation. The cogging torque contributes in mechanical vibration, acoustic noise, torque ripple and hence affects the performance of the machine. These effects are significant and severe for low speed, low inertia and direct drive application. Both techniques i.e., analytical and numerical have been discussed extensively in the literature, however, analytical method of cogging torque calculation is time saving approach and hence, preferable choice for designers. The analytical methods classified as either based on energy variation method, lateral force (LF) method or Maxwell Stress Tensor. The former two methods based on the solution of slotless machine. However, the first method

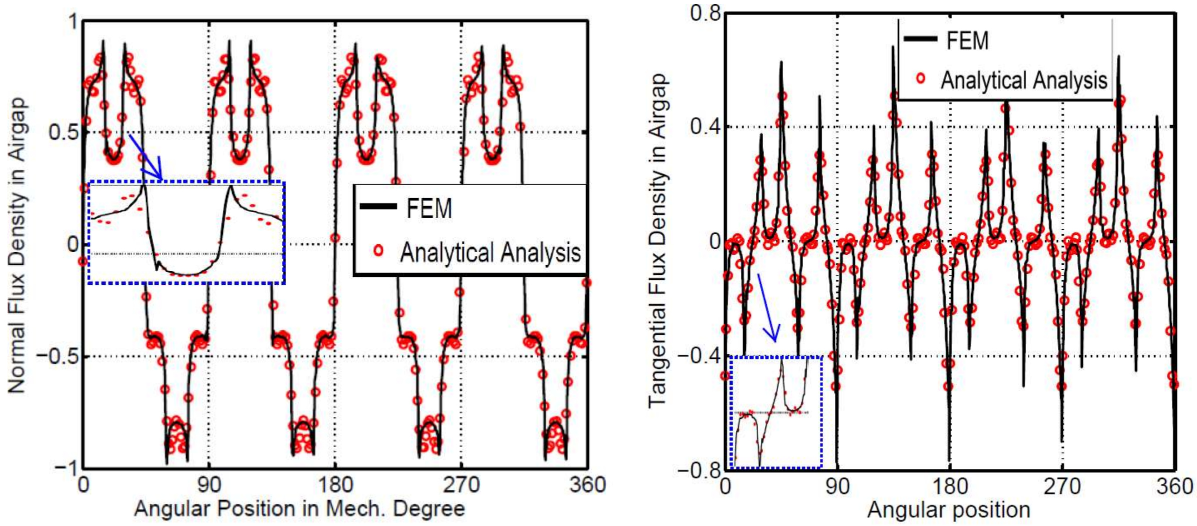

(a) Axial Component (b) Tangential Component

Figure 3.8: Airgap Flux Density Corresponding to $\mu_j = 100$

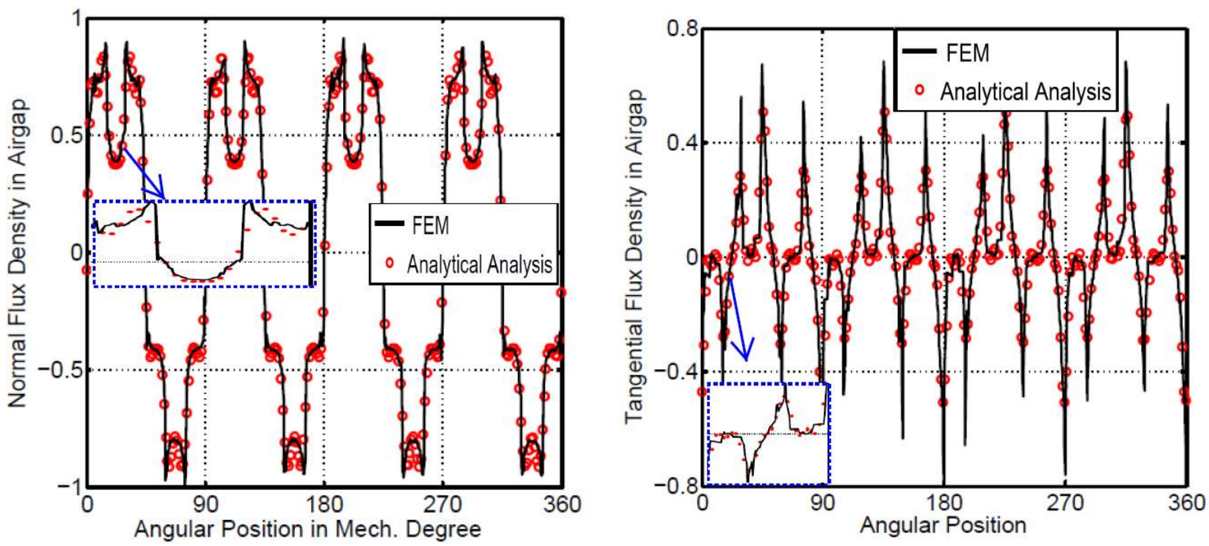

(a) Axial Component (b) Tangential Component

Figure 3.9: Airgap Flux Density Corresponding to $\mu_j = 500$

includes calculation for relative permeance function using Fourier expansion of the airgap permeance [166], [167], calculation of airgap stored magnetic energy. On the other hand, the second method incorporates slot effect using permeance function, obtained from conformal mapping [89], [90], and investigation of cogging torque is based on total moment of magnetic force acting on both slot sides [91]. Several studies suggest that the accuracy of the lateral force method is higher than the energy method [168], [167]. Usually the later method exhibits a larger error in magnitude due to neglecting the energy associated

Table 3.1: Details of AFPM Machine with Saturated Teeth

Machine's Parameters	Values
No of pole Pairs (P)	4
No of Slots (Q)	12
Inner Radius R_i	45 mm
Outer Radius R_0	50 mm
Magnet Height h_m	5 mm
Airgap length g	2 mm
Slot Height h_s	10 mm
Slot Angle α	$\frac{\pi}{Q}$
Teeth Angle β	$\frac{\pi}{Q}$
Magnet Pitch θ_m	π/P
B_r, μ_r	1.1T,1.05
Teeth Relative Permeability μ_i	variable

with the circumferential field component [169]. However, the energy method is powerful technique in analytical determination of optimal design parameters for minimum cogging torque [170]. High accuracy of the cogging torque can be obtained by use of Maxwell stress tensor which involves the subdomain analysis of the no load magnetic field and associated stress developed either on the stator or rotor. All methods briefed above are developed for radial flux machine, however, these are equally applicable for the AFPM machine. In foregoing analysis, the cogging torque in each slice is calculated by the use of Maxwell stress tensor is given by

$$dT = \frac{1}{\mu_o} \int \int_s r \mathbf{B_{2z}} \mathbf{B_{2\theta}} ds \tag{3.28}$$

where B_{2z} and $B_{2\theta}$ are axial and tangential flux density components at PM surface and S is the PMs surface and defined as $ds = rdrd\theta$, which is further simplified as [69]

$$dT = \frac{1}{\mu_o} \int_0^{2\pi} \int_{r_i}^{r_o} r^2 \mathbf{B_{2z}} \mathbf{B_{2\theta}} drd\theta \tag{3.29}$$

where r_i, and r_o are inner and outer radii of the slice of AFPM machine. Hence total cogging torque experienced by the machine is evaluated by use of the algebraic summation

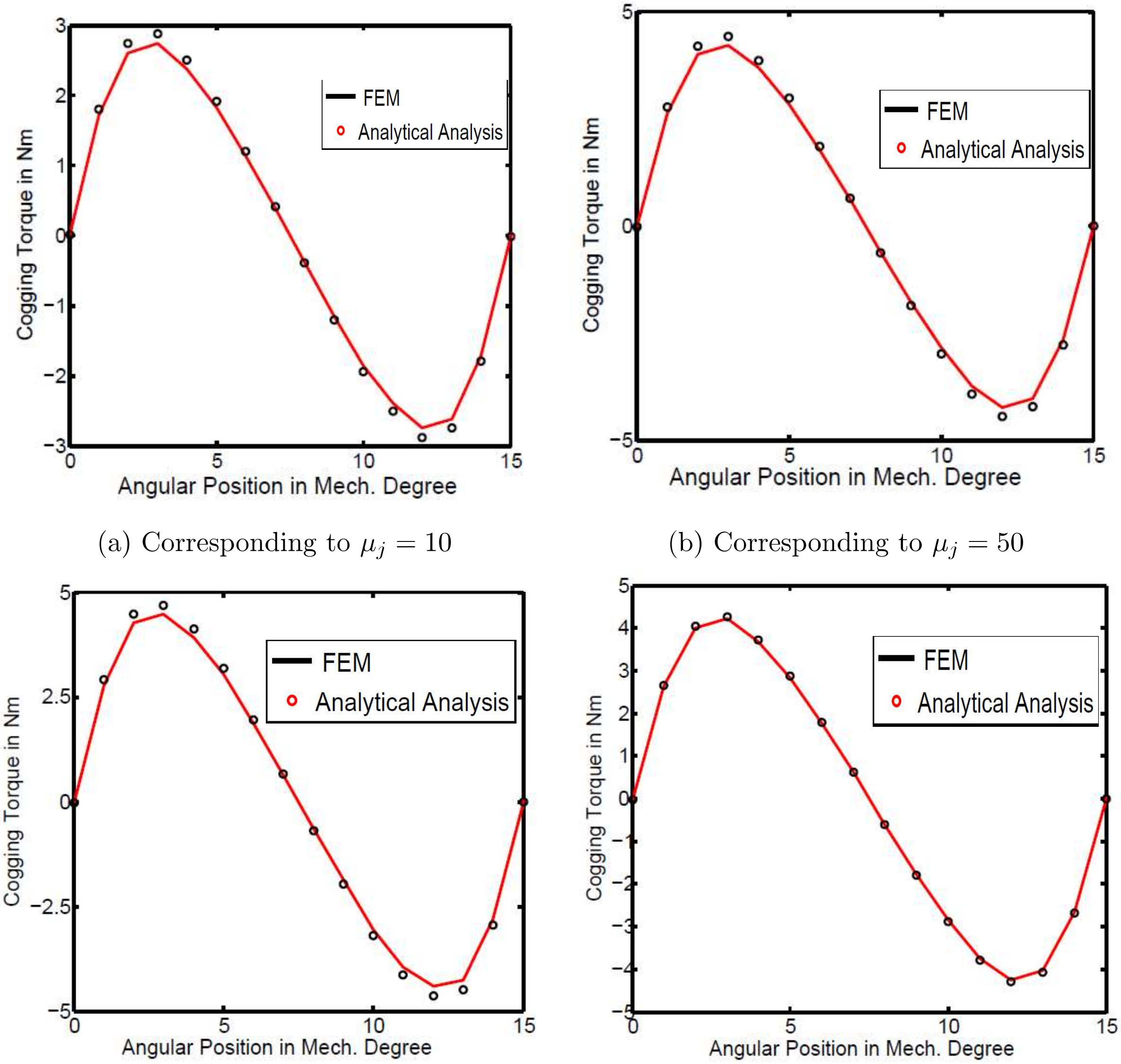

(a) Corresponding to $\mu_j = 10$

(b) Corresponding to $\mu_j = 50$

(c) Corresponding to $\mu_j = 100$

(d) Corresponding to $\mu_j = 500$

Figure 3.10: Comparison of Cogging Torque

of cogging generated by individual slice and expressed as

$$T = \sum_{slice=1}^{Ns} dT \tag{3.30}$$

3.3 Finite Element Analysis and Result Verification

In order to verify the analytical analysis developed in previous section, 3D model of AFPM is simulated in ANSYS MAXWELL 18.0 software as shown in Figure-F.2. The developed model is enclosed within a boundary (region) and Neumann condition is assigned to the boundary. The simulated machine dimensional details are given in the Table 3.1.

To take account of the saturated teeth, four FEM models are developed. Each model considered similar stator yoke and rotor yoke relative permeability as 4000, while the teeth relative permeability are different viz.,μ_i=10, 50, 100, and 500. On the other hand, for the analytical analysis, the machine is divided into 20 slices, and number of harmonics (N_{max}, slot region M_{max}, and slot region K_{max}) considered for the flux density and cogging torque calculation are taken as 50. At the first stage of comparison, the axial and tangnetial components of airgap flux density at radius r=50 mm and z= 7mm are evaluated analytically and compared with the FEM results. The comparison shown in the Figures (3.6), (3.7), (3.8) and (3.9) ensures the correctness of the proposed analysis. Further investigation of cogging torque at different level of magnetic situation of teeth is carried out and their results are compared in Figure-3.10.

3.4 Conclusion

A simplified analytical model for the analysis of saturated axial PM machine is proposed. The comparison of analytical and FEM results are within permissible limits. However, in Figure-3.6 the discrepancy in analytical and FEM results are high. This is because of the assumption that ensures the flux at the edges of the teeth to be tangential. The comparative study of the analytical and FEM results for cogging torque is done at different level of magnetic saturation. The reduces cogging torque is noticed at lower teeth permeabiltiy. It is beacsue of the high airgap relutance and lower airgap flux density at high magnetic saturation.